

Measurement configuration optimization for dynamic metrology using Stokes polarimetry

Jiamin Liu¹, Chuanwei Zhang¹, Zhicheng Zhong, Honggang Gu, Xiuguo Chen², Hao Jiang² and Shiyuan Liu²

State Key Laboratory for Digital Manufacturing Equipment and Technology, Huazhong University of Science and Technology, Wuhan 430074, People's Republic of China

E-mail: hjiang@hust.edu.cn and shyliu@hust.edu.cn

Received 24 October 2017, revised 31 January 2018

Accepted for publication 13 February 2018

Published 16 April 2018



Abstract

As dynamic loading experiments such as a shock compression test are usually characterized by short duration, unrepeatability and high costs, high temporal resolution and precise accuracy of the measurements is required. Due to high temporal resolution up to a ten-nanosecond-scale, a Stokes polarimeter with six parallel channels has been developed to capture such instantaneous changes in optical properties in this paper. Since the measurement accuracy heavily depends on the configuration of the probing beam incident angle and the polarizer azimuth angle, it is important to select an optimal combination from the numerous options. In this paper, a systematic error propagation-based measurement configuration optimization method corresponding to the Stokes polarimeter was proposed. The maximal Frobenius norm of the combinatorial matrix of the configuration error propagating matrix and the intrinsic error propagating matrix is introduced to assess the measurement accuracy. The optimal configuration for thickness measurement of a SiO₂ thin film deposited on a Si substrate has been achieved by minimizing the merit function. Simulation and experimental results show a good agreement between the optimal measurement configuration achieved experimentally using the polarimeter and the theoretical prediction. In particular, the experimental result shows that the relative error in the thickness measurement can be reduced from 6% to 1% by using the optimal polarizer azimuth angle when the incident angle is 45°. Furthermore, the optimal configuration for the dynamic metrology of a nickel foil under quasi-dynamic loading is investigated using the proposed optimization method.

Keywords: Stokes polarimeter, measurement configuration optimization, accuracy, error propagation, dynamic metrology

(Some figures may appear in colour only in the online journal)

1. Introduction

Transient responses of materials under extreme conditions [1] such as high pressure and high temperature, which are usually exhibited under dynamic loadings generated by pulse heating [2], ultrashort pulse laser pumping [3] and flyer-plate impact [4], are of great importance in the study of material physics [5].

¹ Jiamin Liu and Chuanwei Zhang contributed equally to this work.

² Authors to whom any correspondence should be addressed.

Since the duration of the dynamic loading and corresponding response is extremely short, i.e. less than several microseconds, and the kinematic movements and physical or chemical property changes are usually coupled, characterization of such a transient process is very challenging. Moreover, while the cost of such experiments is rather expensive, and the individual experimental process is usually unrepeatably, it is highly desirable to measure the dynamics responses of the sample with fine temporal resolution as well as with high accuracy and precision.

In recent years, many researchers have striven to reveal the dynamic response mechanism of materials under dynamic loadings, and significant progress has been achieved in fast metrology of kinematic responses. Since Barker and Hollenbach proposed a velocity interferometer system for any reflector (VISAR) to measure the velocity history of the free surface in plate-impact experiments in the 1970s [6], VISAR has been applied as an indispensable instrument in gas gun experiments. In 1983, Bloomquist and Sheffield adopted an electronic streak camera to record interference fringe motion in the VISAR [7], which makes it possible to measure the velocity history of the monitored surface with a time resolution of 300 ps. Strand *et al* employed a beat frequency theory to convert the velocimetry of a moving surface to the measurable intensity of an interference beam [8]. Correspondingly, they developed a compact photon Doppler velocimetry (PDV) system to extract the velocity time histories for both the aluminum surface and the LiF surface. Although the kinematic movement of the free surface is accessible with the help of these methods, the metrology of time-dependent physical or chemical properties, which usually reflect the important changes in lattice structure and physical phase, are rarely explored.

Since these properties are difficult to directly acquire under such extreme conditions, an alternative plan would be to analyze the variation of optical constants encoded in the changes in reflectivity [9], phase [10], Raman spectrum [11] and polarization [12]. If the transient refractive indices are accessible, by correlating the time-dependent optical properties to the dynamic changes in the electronic structure or the lattice structure, some microscopic interpretation for the megascopic phase change, ablation and destruction of materials may become appreciable. Rebibo *et al* measured the normalized reflection coefficient and the phase of a laser-pumped polypropylene target by using a single-shot spectral interferometry system [13], in which the sensitivity of the refractive index of the laser-breakdown target to the electron density rise has been investigated. In 2008, Bolme *et al* developed an ultrafast dynamic ellipsometer (UDE) to measure the shocked refractive indices of a polycarbonate [14], which successfully decoupled the dynamic optical constant changes and the kinematic movements of the free surface. Since the UDE proposed by Bolme *et al* has adopted a femtosecond laser as the source, the equipment is rather expensive and picky in working conditions. Recently, a full Stokes vector ellipsometry system built by Bakshi *et al* showed an attractive example of measuring refractive index changes due to its reasonable cost and potential for high temporal resolution [15].

Similar to ellipsometry, the performance of the Stokes polarimeter heavily depends on the measurement configuration [16], which usually consists of the probing beam incident angle and polarizer azimuth angle. Configuration optimization is a feasible way to improve both accuracy and precision of the measurement. Currently, the configuration optimization methods can be roughly classified into two categories according to their objectives. The first is for optimizing the system matrix of the instrument based on the determinant and condition number [17–19], singular value decomposition [20]

or the Eulerian length [21], with the objective of improving the quality of measured data. Since the systematic errors are difficult to eliminate completely in the measured signature, ignoring the influence of residue systematic error may significantly degrade the accuracy and precision of the measurements. The second is the sensitivity analysis-based measurement configuration optimization method, the objective of which is to ensure the precision or accuracy of the measurement results; it was first introduced in optical critical dimension metrology using a scatterometer [22–25]. In the sensitivity-based method, it is assumed that the instrument has been perfectly calibrated, therefore, the influence of configuration errors or the intrinsic errors are usually ignored. However, careful calibration of the instrument can only partially eliminate the sources of errors, and it is necessary to consider the complete error propagation in measurement configuration optimization.

In this paper, a Stokes polarimeter with six parallel detection channels has been developed. We first derive the corrected formula for Stokes vector calculation by taking the error induced by beam splitters into consideration. Then, a measurement configuration optimization model has been proposed based on the systematic error propagation mechanism [26]. In the optimization model, the measurement configuration consists of the incident angle and polarization state of the probing beam, and the objective function is defined as the maximal Frobenius norm of the combinatorial matrix of the configuration error propagating matrix and the intrinsic error propagating matrix. By minimizing the objective function in the feasible configuration domain, the optimal configuration can be achieved. The virtual and practical measurement experiments on a SiO₂ thin film sample have been sequentially carried out for demonstration. Furthermore, we investigate the optimal configuration for the measurement of a nickel foil under dynamic loading using the proposed method.

2. Principle and instrument

A Stokes polarimeter with six parallel detection channels has been developed to capture the instantaneous changes in optical constants of materials under dynamic loadings. As schematically shown in figure 1(a), the system settings of the instrument in order of light propagation are P₁C₁P₂SA, where P₁, C₁, P₂, S and A stand for the first polarizer, a quarter-wave plate, the second polarizer, the sample and the analyzing module, respectively. Since the probing beam produced by a laser is usually a polarized light with high intensity, the first polarizer P₁ acts as a diattenuator to decay the intensity to an appropriate range. The second polarizer P₂ acts as a polarization generator to change the probing beam to an expected linear polarized light. In order to avoid the extinction effect caused by the different azimuth angles of the two polarizers, a quarter-wave plate C₁ has been inserted between the two polarizers. The difference between the azimuth angles of the first polarizer P₁ and of the quarter-wave plate C₁ is set as 45°. Accordingly, the polarization of the probing beam is modulated sequentially by the first polarizer P₁ and the quarter-wave

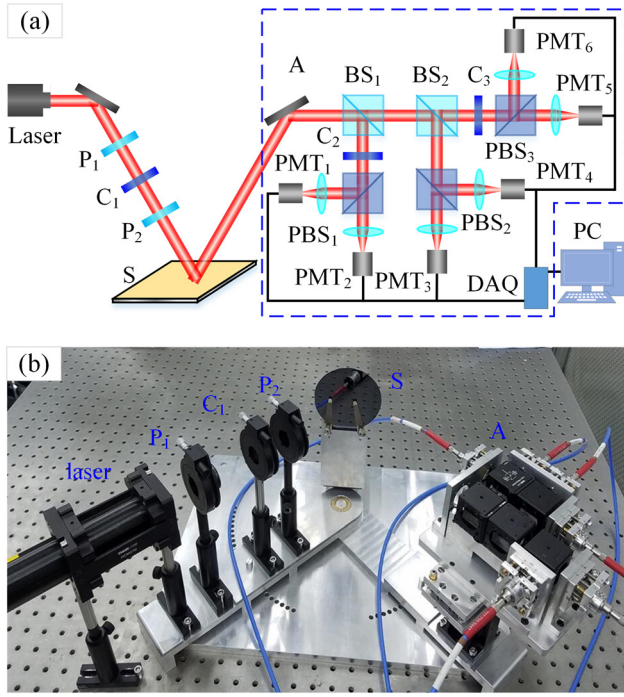


Figure 1. (a) Schematic and (b) prototype of the Stokes polarimeter. P_1 and P_2 , polarizers; C_1 and C_2 , quarter-wave plates; C_3 , half-wave plate; S , sample; A , analyzing module; BS_1 and BS_2 , beam splitters; PBS_1 , PBS_2 and PBS_3 , polarization beam splitters; PMT_1 , PMT_2 , PMT_3 , PMT_4 , PMT_5 and PMT_6 , photomultiplier tubes; DAQ, oscilloscope; PC, personal computer.

plate C_1 is the right-circular polarization. Then, the intensity of the probing beam modulated by the second polarizer P_2 is always identical at arbitrary azimuth angles of the second polarizer, which is convenient and ensures the accuracy for the calibration of the Stokes polarimeter. Meanwhile, the feasible azimuth angle domain of the second polarizer has been also expanded when compared to the one of the setup without the quarter-wave plate C_1 . The analyzing module consists of two beam splitters BS_1 and BS_2 with split ratios of 3:7 and 5:5, respectively, a quarter-wave plate C_2 , a half-wave plate C_3 , three polarization beam splitters PBS_1 , PBS_2 and PBS_3 and six photomultiplier tubes PMT_1 – PMT_6 .

Supposing the Stokes vector of the light source is $\mathbf{S}_{in} = [1, 1, 0, 0]^T$, the Stokes vector \mathbf{S}_{ref} of the light beam reflected by the sample surface can be expressed as a Mueller matrix product shown in equation (1) [27]

$$\mathbf{S}_{ref} = \mathbf{M}_S [\mathbf{R}(-\alpha_2) \mathbf{M}_{P_2} \mathbf{R}(\alpha_2)] [\mathbf{R}(-\beta_1) \mathbf{M}_{C_1}(90^\circ) \mathbf{R}(\beta_1)] [\mathbf{R}(-\alpha_1) \mathbf{M}_{P_1} \mathbf{R}(\alpha_1)] \mathbf{S}_{in}, \quad (1)$$

where \mathbf{M}_i ($i = P_1, C_1, P_2$) is the Mueller matrix associated with each optical element, \mathbf{M}_S is the Mueller matrix of the sample, and $\mathbf{R}(x)$ is the Mueller rotation transformation matrix for rotation by the angle x ($x = \alpha_1, \beta_1, \alpha_2$), which is the azimuth angle of each corresponding element. We set β_1 as $\alpha_1 + 45^\circ$ here to achieve a right-circularly polarized incident light before modulation by P_2 .

In the analyzing module, two beam splitters divide the reflected light into three beam branches. The first beam branch is demodulated sequentially by the quarter-wave plate

C_2 and the polarization beam splitter PBS_1 , and the second beam branch is demodulated directly by the polarization beam splitter PBS_2 . The third beam branch is demodulated sequentially by the half-wave plate C_3 and the polarization beam splitter PBS_3 . Since the polarization beam splitter can divide an arbitrary polarization beam into two components, i.e. the p- and s-components, the reflected light is eventually divided into six sub-beams after being demodulated by the analyzing module. The light intensities ($I_j, j = 1-6$) of these six channels are detected by the photomultiplier tubes PMT_1 – PMT_6 and can be expressed as equation (2):

$$I_1 = k_1 \cdot \begin{bmatrix} 1 & 0 & 0 & 0 \end{bmatrix} \cdot \left[\mathbf{R}(-0^\circ) \mathbf{M}_{PBS_1} \mathbf{R}(0^\circ) \right] \times \left[\mathbf{R}(-\beta_2) \mathbf{M}_{C_2}(90^\circ) \mathbf{R}(\beta_2) \right] \Gamma_{BS_1} \mathbf{S}_{ref}, \quad (2.1)$$

$$I_2 = k_2 \cdot \begin{bmatrix} 1 & 0 & 0 & 0 \end{bmatrix} \cdot \left[\mathbf{R}(-90^\circ) \mathbf{M}_{PBS_1} \mathbf{R}(90^\circ) \right] \times \left[\mathbf{R}(-\beta_2) \mathbf{M}_{C_2}(90^\circ) \mathbf{R}(\beta_2) \right] \Gamma_{BS_1} \mathbf{S}_{ref}, \quad (2.2)$$

$$I_3 = k_3 \cdot \begin{bmatrix} 1 & 0 & 0 & 0 \end{bmatrix} \cdot \left[\mathbf{R}(-0^\circ) \mathbf{M}_{PBS_2} \mathbf{R}(0^\circ) \right] \Gamma_{BS_2} \Lambda_{BS_1} \mathbf{S}_{ref}, \quad (2.3)$$

$$I_4 = k_4 \cdot \begin{bmatrix} 1 & 0 & 0 & 0 \end{bmatrix} \cdot \left[\mathbf{R}(-90^\circ) \mathbf{M}_{PBS_2} \mathbf{R}(90^\circ) \right] \Gamma_{BS_2} \Lambda_{BS_1} \mathbf{S}_{ref}, \quad (2.4)$$

$$I_5 = k_5 \cdot \begin{bmatrix} 1 & 0 & 0 & 0 \end{bmatrix} \cdot \left[\mathbf{R}(-0^\circ) \mathbf{M}_{PBS_3} \mathbf{R}(0^\circ) \right] \times \left[\mathbf{R}(-\beta_3) \mathbf{M}_{C_3}(180^\circ) \mathbf{R}(\beta_3) \right] \Lambda_{BS_2} \Lambda_{BS_1} \mathbf{S}_{ref}, \quad (2.5)$$

$$I_6 = k_6 \cdot \begin{bmatrix} 1 & 0 & 0 & 0 \end{bmatrix} \cdot \left[\mathbf{R}(-90^\circ) \mathbf{M}_{PBS_3} \mathbf{R}(90^\circ) \right] \times \left[\mathbf{R}(-\beta_3) \mathbf{M}_{C_3}(180^\circ) \mathbf{R}(\beta_3) \right] \Lambda_{BS_2} \Lambda_{BS_1} \mathbf{S}_{ref}, \quad (2.6)$$

where k_j ($j = 1-6$) is the gain of the j th parallel channel, \mathbf{M}_l ($l = C_2, C_3, PBS_1, PBS_2, PBS_3$) is the Mueller matrices associated with the optical elements corresponding to the subscripts. β_2 and β_3 are the azimuth angles of the quarter-wave plate C_2 and the half-wave plate C_3 , respectively. Γ and Λ are the reflected and the transmitted Mueller matrices corresponding to the beam splitter subscripted.

Assuming that the beam splitters are ideal non-polarized elements, the Mueller matrices Γ_m ($m = BS_1, BS_2$) and Λ_m ($m = BS_1, BS_2$) of the beam splitters can be expressed as equation (3) [28]:

$$\Gamma_m = \begin{bmatrix} 1 & 0 & 0 & 0 \\ 0 & 1 & 0 & 0 \\ 0 & 0 & u & 0 \\ 0 & 0 & 0 & u \end{bmatrix} \quad m = BS_1, BS_2, \quad (3.1)$$

$$\Lambda_m = \begin{bmatrix} 1 & 0 & 0 & 0 \\ 0 & 1 & 0 & 0 \\ 0 & 0 & v & 0 \\ 0 & 0 & 0 & v \end{bmatrix} \quad m = BS_1, BS_2, \quad (3.2)$$

where u and v are in the interval of $[-1, 1]$.

Submitting equations (2) and (3), when the azimuth angles of C_2 and C_3 are set as -45° and 22.5° , the Stokes parameters can be expressed as equation (4):

$$S_1/S_0 = \frac{I_3/k_3 - I_4/k_4}{I_3/k_3 + I_4/k_4}, \quad (4.1)$$

$$S_2/S_0 = \frac{I_5/k_5 - I_6/k_6}{I_5/k_5 + I_6/k_6}, \quad (4.2)$$

$$S_3/S_0 = \frac{I_2/k_2 - I_1/k_1}{I_2/k_2 + I_1/k_1}, \quad (4.3)$$

where S_p ($p = 0-3$) is the p th Stokes parameter in \mathbf{S}_{ref} .

According to the definition of the Stokes vector [27], the normalized Stokes vector of the reflective beam for a perfect system can be calculated by equation (4). However, due to the imperfect manufacturing, the polarization effects induced by optical elements such as beam splitters are inevitable and cannot be ignored. We measured the practical Mueller matrices of these optical elements particularly with the inclusion of the beam splitters using a commercial Mueller matrix ellipsometer (ME-L, Wuhan Eoptics Technology Co. Ltd Wuhan, China). The corresponding measured results are shown as equation (5):

$$\mathbf{\Gamma}_{\text{BS}_1} = \begin{bmatrix} 1.0000 & 0.0548 & 0.0005 & 0.0001 \\ 0.0550 & 0.9931 & 0.0003 & -0.0088 \\ 0.0005 & 0.0025 & -0.8488 & 0.5089 \\ -0.0004 & -0.0068 & -0.5083 & -0.8505 \end{bmatrix}$$

$$\mathbf{\Lambda}_{\text{BS}_1} = \begin{bmatrix} 1.0000 & -0.0152 & -0.0006 & -0.0003 \\ -0.0147 & 0.9993 & -0.0040 & -0.0069 \\ -0.0004 & 0.0020 & 0.9958 & -0.0824 \\ -0.0006 & -0.0068 & -0.0822 & 0.9969 \end{bmatrix}$$

$$\mathbf{S}_{\text{meas}} = (\mathbf{B}^T \mathbf{B})^{-1} \mathbf{B}^T \mathbf{I}, \quad (8)$$

where \mathbf{S}_{meas} is the measured Stokes vector of the reflective light from the sample.

The prototype of the Stokes polarimeter built in conformity to the schematic shown in figure 1(a) is shown in figure 1(b). The light source is a CW He-Ne laser (HNL050LB 100-240VAC, Thorlabs, USA) with a wavelength of 632.8nm and a maximum power of 5 mW. The two linear polarizers (LPVISB100-MP2, Thorlabs, USA) with extinction ratios larger than 10000:1 and an achromatic quarter-wave plate (AQWP05M-600, Thorlabs, USA) are used as the beam polarization generator, which can produce a linear polarized light with an appropriate intensity. Since these optical components are mounted on the precision rotation mounts (PRM1/M, Thorlabs, USA), the azimuth angles of polarizers' transmission axes and a wave-plate's fast axis can be adjusted precisely. In the analyzing module, the two beam splitters (BS019 and BS013, Thorlabs, USA) with the split ratios of 3:7 and 5:5 (reflection: transmission) divide the power of the reflected beam into three branches equally. The quarter-wave plate (WPMQ05M-633, Thorlabs, USA) and half-wave plate (WPMH05M-633, Thorlabs, USA) are used in the first and third branches, respectively, and the azimuth angles of their

$$\mathbf{\Gamma}_{\text{BS}_2} = \begin{bmatrix} 1.0000 & -0.0204 & -0.0002 & 0.0007 \\ -0.0206 & 0.9989 & -0.0035 & -0.0088 \\ -0.0005 & 0.0019 & -0.7707 & 0.6343 \\ -0.0006 & -0.0087 & -0.6343 & -0.7718 \end{bmatrix} \quad (5.1)$$

$$\mathbf{\Lambda}_{\text{BS}_2} = \begin{bmatrix} 1.0000 & 0.0061 & -0.0005 & -0.0002 \\ -0.0061 & 0.9999 & -0.0014 & -0.0027 \\ -0.0001 & -0.0010 & 0.9681 & -0.2499 \\ -0.0000 & 0.0029 & 0.2512 & 0.9669 \end{bmatrix}. \quad (5.2)$$

Meanwhile, equation (2) can be modified as a matrix form, shown as equation (6),

$$\mathbf{I} = \left[\frac{I_1}{k_1} \quad \frac{I_2}{k_2} \quad \frac{I_3}{k_3} \quad \frac{I_4}{k_4} \quad \frac{I_5}{k_5} \quad \frac{I_6}{k_6} \right]^T = \mathbf{B} \cdot \mathbf{S}_{\text{ref}}, \quad (6)$$

where \mathbf{I} is the normalized light intensity vector. The instrument matrix \mathbf{B} is calculated from the practical Mueller matrices of these optical elements, as shown in equation (7):

$$\mathbf{B} = \begin{bmatrix} 0.9913 & 0.9899 & -0.0067 & -0.0100 \\ 1.0085 & -1.0081 & 0.0046 & 0.0089 \\ 0.9997 & -0.0310 & -0.7160 & 0.6964 \\ 1.0008 & 0.0403 & 0.7147 & -0.6952 \\ 0.9996 & 0.0480 & -0.5078 & -0.8504 \\ 1.0004 & 0.0616 & 0.5088 & 0.8505 \end{bmatrix}.$$

(7)

Thus, the calculation of the reflected Stokes vector can be modified as equation (8),

fast axes are set as -45° and 22.5° . Thus, the Stokes parameters S_3 and S_2 of the reflected beam can be separated out, respectively. At the end of these three branches, three polarizing beam splitter cubes are used as the beam polarization analyzers (CCM1-PBS25-633/M, Thorlabs, USA). Since the photomultiplier tubes (H10721 Series, Hamamatsu, Japan) and an oscilloscope (WaveSurfer-3000, Teledyne Lecroy, USA) are used as the detection module, which possesses a temporal resolution possesses of up to a ten-nanosecond level, it is possible to capture the transient changes in optical constants of materials under dynamic loadings such as pulse heating.

3. Optimization of measurement configuration

During the measurement process, the reflected Stokes vector \mathbf{S}_{ref} only depends on the Mueller matrix of the sample when the azimuth angles α_2 of the second polarizer

are fixed. According to the Fresnel reflection [27], the reflected Stokes parameter is usually a transcendental function of the measurands. Then, a weighted least-squares regression analysis is introduced to extract the measurands of the sample [29]. The corresponding computing formula is shown as equation (9),

$$\hat{\mathbf{x}} = \underset{\mathbf{x} \in \Omega}{\operatorname{argmin}} \{ \chi^2 \} = \underset{\mathbf{x} \in \Omega}{\operatorname{argmin}} \left\{ \sum_{q=1}^{N_t} \sum_{p=0}^3 \left[\frac{S_{p,q}^{\text{meas}} - S_{p,q}^{\text{calc}}(\mathbf{x}, \mathbf{a})}{\sigma(S_{p,q}^{\text{calc}})} \right]^2 \right\}, \quad (9)$$

where q indicates the q th time point from the total number N_t , and the subscript index p shows the p th Stokes parameters. The variable $S_{p,q}^{\text{meas}}$ is the normalized measured Stokes parameter calculated by equation (8), $S_{p,q}^{\text{calc}}(\mathbf{x}, \mathbf{a})$ is the normalized calculated Stokes parameter calculated by equation (1) and is associated with the measurands vector \mathbf{x} and the measurement configuration vector \mathbf{a} . Since the wavelength λ has been fixed at 632.8 nm and the time points t_q are varied in a specific measurement time range, the configuration parameters vector \mathbf{a} only contains the incidence angle θ of the probing beam and the azimuth angle φ of polarizer P₂, i.e. $\mathbf{a} = [\theta, \varphi]^T$. The variable $\sigma(S_{p,q}^{\text{calc}})$ is the estimated standard deviation associated with $S_{p,q}^{\text{calc}}$, Ω denotes the associated parameter domain of \mathbf{x} and $\hat{\mathbf{x}}$ is the extracted vector of measurand \mathbf{x} .

The normalized measured Stokes parameter $S_{p,q}^{\text{meas}}$ and the normalized calculated Stokes parameters $S_{p,q}^{\text{calc}}(\mathbf{x}, \mathbf{a})$ can be marked as two vectors \mathbf{S} and $\mathbf{S}(\mathbf{x}, \mathbf{a})$, respectively. The overall standard deviation $\sigma(S_{p,q}^{\text{calc}})$ can be recorded as an $N \times N$ diagonal weighting matrix \mathbf{W} ($N = 4N_t$). Then, the weighted mean-square error function χ^2 defined in equation (9) can be simply rewritten as equation (10),

$$\chi^2 = [\mathbf{S} - \mathbf{S}(\mathbf{x}, \mathbf{a}^*)]^T \mathbf{W} [\mathbf{S} - \mathbf{S}(\mathbf{x}, \mathbf{a}^*)], \quad (10)$$

where \mathbf{a}^* denotes the given measurement configuration vector.

Suppose the normalized calculated Stokes parameter vector $\mathbf{S}(\mathbf{x}, \mathbf{a})$ is a smooth function and can be expanded in a first-order Taylor series at $(\hat{\mathbf{x}}, \mathbf{a}^*)$:

$$\begin{aligned} \mathbf{S}(\mathbf{x}_0, \mathbf{a}_0) &= \mathbf{S}(\hat{\mathbf{x}}, \mathbf{a}^*) + \mathbf{J}_x \cdot (\mathbf{x}_0 - \hat{\mathbf{x}}) + \mathbf{J}_a \cdot (\mathbf{a}_0 - \mathbf{a}^*) \\ &= \mathbf{S}(\hat{\mathbf{x}}, \mathbf{a}^*) + \mathbf{J}_x \cdot \Delta \mathbf{x} + \mathbf{J}_a \cdot \Delta \mathbf{a}, \end{aligned} \quad (11)$$

where \mathbf{x}_0 and \mathbf{a}_0 are the true value vectors of \mathbf{x} and \mathbf{a} , respectively and \mathbf{J}_x and \mathbf{J}_a are the $N \times M$ and $N \times 2$ Jacobian matrices with respect to \mathbf{x} and \mathbf{a} , respectively. The variable $\Delta \mathbf{x}$ represents the error propagated into $\hat{\mathbf{x}}$, and $\Delta \mathbf{a}$ is the configuration parameters error.

Usually, a normalized measured Stokes parameter vector \mathbf{S} consists of the true signature, the intrinsic error as well as the random error [30], which can be expressed as equation (12),

$$\mathbf{S} = \mathbf{S}(\mathbf{x}_0, \mathbf{a}_0) + \boldsymbol{\mu}_S + \boldsymbol{\varepsilon}_S, \quad (12)$$

where $\mathbf{S}(\mathbf{x}_0, \mathbf{a}_0)$ is the true Stokes parameter vector of the sample. The intrinsic error $\boldsymbol{\mu}_S$ and the random error $\boldsymbol{\varepsilon}_S$ in Stokes parameters are induced by the biases in the systematic parameters of the instrument matrix \mathbf{B} and the random noise in the normalized measured light intensity \mathbf{I} , respectively.

After inserting equations (11) and (12) into equation (10), the weighted mean-square error function χ^2 can be modified as equation (13):

$$\begin{aligned} \chi^2 &= [\mathbf{S}(\hat{\mathbf{x}}, \mathbf{a}^*) + \mathbf{J}_x \cdot \Delta \mathbf{x} + \mathbf{J}_a \cdot \Delta \mathbf{a} + \boldsymbol{\mu}_S + \boldsymbol{\varepsilon}_S - \mathbf{S}(\mathbf{x}, \mathbf{a}^*)]^T \\ &\quad \mathbf{W} [\mathbf{S}(\hat{\mathbf{x}}, \mathbf{a}^*) + \mathbf{J}_x \cdot \Delta \mathbf{x} + \mathbf{J}_a \cdot \Delta \mathbf{a} + \boldsymbol{\mu}_S + \boldsymbol{\varepsilon}_S - \mathbf{S}(\mathbf{x}, \mathbf{a}^*)]. \end{aligned} \quad (13)$$

Considering that $\hat{\mathbf{x}}$ is the extracted value vector from a weighted least-squares regression analysis shown as equation (9), the error function χ^2 should have a minimum at $\hat{\mathbf{x}}$:

$$\begin{aligned} \chi_{\min}^2 &= [\mathbf{J}_x \cdot \Delta \mathbf{x} + \mathbf{J}_a \cdot \Delta \mathbf{a} + \boldsymbol{\mu}_S + \boldsymbol{\varepsilon}_S]^T \\ &\quad \mathbf{W} [\mathbf{J}_x \cdot \Delta \mathbf{x} + \mathbf{J}_a \cdot \Delta \mathbf{a} + \boldsymbol{\mu}_S + \boldsymbol{\varepsilon}_S]. \end{aligned} \quad (14)$$

Theoretically, the minimum of the error function χ^2 is equal or very close to zero. By taking the arithmetic square root of both sides of equation (14), an error propagating formula can be obtained as shown in equation (15):

$$\mathbf{W}^{1/2} \cdot [\mathbf{J}_x \cdot \Delta \mathbf{x} + \mathbf{J}_a \cdot \Delta \mathbf{a} + \boldsymbol{\mu}_S + \boldsymbol{\varepsilon}_S] \approx 0. \quad (15)$$

Furthermore, equation (15) can be expanded to the following form as shown in equation (16),

$$\mathbf{W}^{1/2} \mathbf{J}_x \cdot (\boldsymbol{\mu}_x + \boldsymbol{\varepsilon}_x) + \mathbf{W}^{1/2} \mathbf{J}_a \cdot \Delta \mathbf{a} + \mathbf{W}^{1/2} \boldsymbol{\mu}_S + \mathbf{W}^{1/2} \boldsymbol{\varepsilon}_S \approx 0, \quad (16)$$

where $\boldsymbol{\mu}_x$ and $\boldsymbol{\varepsilon}_x$ are the systematic error and the random error propagated into $\hat{\mathbf{x}}$, respectively.

Since both the averages of $\boldsymbol{\varepsilon}_S$ and $\boldsymbol{\varepsilon}_x$ are equal to zero, the systematic error propagating formula can be derived by taking the average of equation (16),

$$-\boldsymbol{\mu}_x = \left[\begin{array}{cc} (\mathbf{J}_x^T \mathbf{W} \mathbf{J}_x)^{-1} \mathbf{J}_x^T \mathbf{W} \mathbf{J}_a & (\mathbf{J}_x^T \mathbf{W} \mathbf{J}_x)^{-1} \mathbf{J}_x^T \mathbf{W} \end{array} \right] \cdot \begin{bmatrix} \Delta \mathbf{a} \\ \boldsymbol{\mu}_S \end{bmatrix}, \quad (17)$$

where $(\mathbf{J}_x^T \mathbf{W} \mathbf{J}_x)^{-1} \mathbf{J}_x^T \mathbf{W} \mathbf{J}_a$ and $(\mathbf{J}_x^T \mathbf{W} \mathbf{J}_x)^{-1} \mathbf{J}_x^T \mathbf{W}$ are the propagation coefficient matrices of the configuration error $\Delta \mathbf{a}$ and the intrinsic error $\boldsymbol{\mu}_S$, respectively.

Equation (17) suggests that both the effects of the configuration parameter errors and the intrinsic errors of the measured Stokes parameters should be taken into consideration in the measurement error evaluation. After taking the Frobenius norm on both sides of equation (17),

$$\|\boldsymbol{\mu}_x\|_F = \left\| \left[\begin{array}{cc} (\mathbf{J}_x^T \mathbf{W} \mathbf{J}_x)^{-1} \mathbf{J}_x^T \mathbf{W} \mathbf{J}_a & (\mathbf{J}_x^T \mathbf{W} \mathbf{J}_x)^{-1} \mathbf{J}_x^T \mathbf{W} \end{array} \right] \right\|_F \cdot \left\| \begin{bmatrix} \Delta \mathbf{a} \\ \boldsymbol{\mu}_S \end{bmatrix} \right\|_F, \quad (18)$$

where $\|\boldsymbol{\mu}_x\|_F$ is equivalent to the magnitude of the systematic error $\boldsymbol{\mu}_x$ in the measurands, $\left\| \begin{bmatrix} \Delta \mathbf{a} \\ \boldsymbol{\mu}_S \end{bmatrix} \right\|_F$ is equivalent to the magnitude of the configuration error $\Delta \mathbf{a}$ and the intrinsic error $\boldsymbol{\mu}_S$ of the instrument and $\left\| \left[\begin{array}{cc} (\mathbf{J}_x^T \mathbf{W} \mathbf{J}_x)^{-1} \mathbf{J}_x^T \mathbf{W} \mathbf{J}_a & (\mathbf{J}_x^T \mathbf{W} \mathbf{J}_x)^{-1} \mathbf{J}_x^T \mathbf{W} \end{array} \right] \right\|_F$ are the amplification factors.

Considering that the instrument has been well calibrated, the magnitude of the configuration parameter errors $\Delta \mathbf{a}$ and the intrinsic errors $\boldsymbol{\mu}_S$ are nearly invariable, whereas the magnitude of $\left\| \left[\begin{array}{cc} (\mathbf{J}_x^T \mathbf{W} \mathbf{J}_x)^{-1} \mathbf{J}_x^T \mathbf{W} \mathbf{J}_a & (\mathbf{J}_x^T \mathbf{W} \mathbf{J}_x)^{-1} \mathbf{J}_x^T \mathbf{W} \end{array} \right] \right\|_F$ is

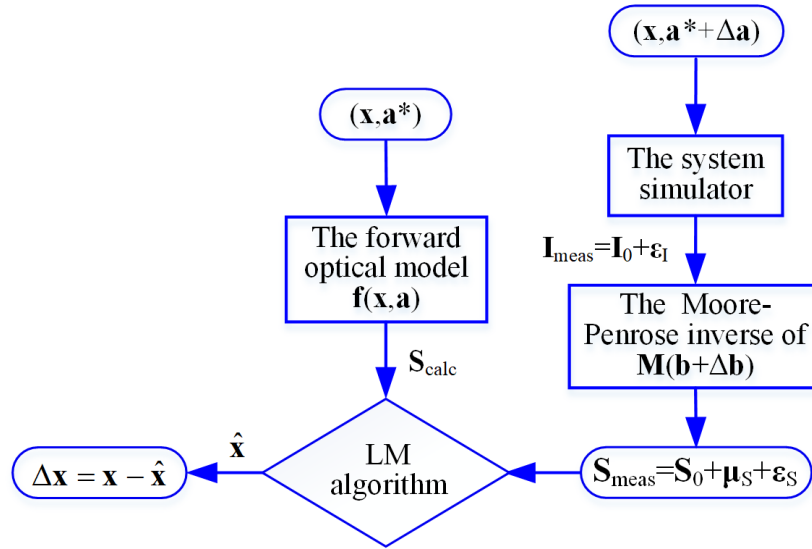


Figure 2. The operational procedures for the virtual measurement experiment of the polarimeter.

highly dependent on the measurement configurations. Thus, the smallest value of the systematic error μ_x can be achieved by finding an appropriate configuration \mathbf{a} . The corresponding objective function for measurement configuration optimization, which is used to pick out the minimum amplification factors, can be defined as equation (19),

$$(\theta_{\text{opt}}, \varphi_{\text{opt}}) = \arg \min_{\theta \in \Phi, \varphi \in H} \left\{ \max_{x \in \Omega} \left[\left\| \left[\left(\mathbf{J}_x^T \mathbf{W} \mathbf{J}_x \right)^{-1} \mathbf{J}_x^T \mathbf{W} \mathbf{J}_a \quad \left(\mathbf{J}_x^T \mathbf{W} \mathbf{J}_x \right)^{-1} \mathbf{J}_x^T \mathbf{W} \right] \right\|_F \right] \right\}, \quad (19)$$

where Φ and H are the value space of the incident angle of the probing beam and the azimuth angle of the polarizer P_2 , respectively.

4. Results and discussion

In this section, we first validate the systematic error propagating formula of the instrument using a virtual experiment. Then, an experimental test on a standard SiO_2 thin film is conducted and the consistency between the optimal configuration exhibited in the experiment and the theoretical prediction is checked for demonstration. Finally, a simulation of measuring a nickel foil under dynamic loading is conducted and the optimal configuration for such a dynamic application is suggested.

In the first test case, the static measurement on a standard SiO_2 thin film with nominal thickness of 32 nm deposited on a Si substrate was simulated following the procedures shown in figure 2. A simulator of the polarimeter was first built based on equations (1) and (2) to simulate the measurement process. Then, the measurands vector \mathbf{x} and the measurement configuration vector $\mathbf{a}^* + \Delta \mathbf{a}$ were selected as the input arguments, and the measured light intensity vector \mathbf{I}_{meas} was calculated using equation (6). The light intensity vector \mathbf{I}_{meas} consists of the pure calculated intensity vector \mathbf{I}_0 and the random noise ϵ_1 obtained from a signal-dependent noise generator [31]. Subsequently, the imitated measured Stokes parameters \mathbf{S}_{meas} can be calculated using equation (8). At this point, the

instrument matrix of the polarimeter is $\mathbf{M}(\mathbf{b} + \Delta \mathbf{b})$. The vectors \mathbf{b} and $\Delta \mathbf{b}$ are the systematic parameters and the corresponding bias of the polarimeter, respectively. The vector \mathbf{b} consists of the phase retardance and the fast axis azimuth angles of the quarter-wave plates C_2 and the half-wave plate C_3 in the analyzing module. The estimated measurands $\hat{\mathbf{x}}$ can be extracted from the imitated Stokes parameters \mathbf{S}_{meas} with the configuration \mathbf{a}^* based on the Levenberg Marquardt algorithm [32].

In figure 2, the measurand \mathbf{x} is set as the thickness of an SiO_2 layer whose nominal value is 32 nm. The incidence angle θ is varied from 51° to 69° with an increment of 6° , and the polarizer azimuth angle φ is varied from 15° to 80° with an increment of 5° . The systematic parameters in the system model of the polarimeter are set as $\mathbf{b} = [22.5^\circ, 180^\circ, -45^\circ, 90^\circ]^T$. The configuration error and the bias of systematic parameters are set as $\Delta \mathbf{a} = [\Delta \theta, \Delta \varphi]^T = [0.1^\circ, 0.1^\circ]^T$ and $\Delta \mathbf{b} = [0.1^\circ, 0.1^\circ, 0.1^\circ, 0.1^\circ]^T$, respectively. The virtual measurement experiment was implemented 200 times to obtain a series of imitated measured Stokes parameters \mathbf{S}_{meas} and a series of imitated errors $\Delta \mathbf{x}$ propagated into $\hat{\mathbf{x}}$. Taking the average of the errors series, the imitated systematic error $\langle \Delta \mathbf{x} \rangle$ propagated into $\hat{\mathbf{x}}$ and the average $\langle \mathbf{S}_{\text{meas}} \rangle$ of the imitated measured Stokes parameters can be obtained. Meanwhile, the imitated true signature \mathbf{S}_0 in \mathbf{S}_{meas} can be also obtained from the forward optical model $\mathbf{f}(\mathbf{x}, \mathbf{a})$ with the input arguments \mathbf{x} and $\mathbf{a}^* + \Delta \mathbf{a}$. Therefore, the imitated intrinsic error μ_S of Stokes parameters \mathbf{S}_{meas} can be calculated from equation (20):

$$\mu_S = \langle \mathbf{S}_{\text{meas}} \rangle - \mathbf{S}_0 = \langle \mathbf{S}_{\text{meas}} \rangle - \mathbf{f}(\mathbf{x}, \mathbf{a}^* + \Delta \mathbf{a}). \quad (20)$$

Correspondingly, the calculated error μ_x can be obtained from equation (17) with the given configuration error $\Delta \mathbf{a}$ above. Then, the comparison between the imitated systematic error $\langle \Delta \mathbf{x} \rangle$ and the calculated systematic error μ_x are shown in figure 3. We find that some correlations exist between the absolute errors in thickness measurement and the polarizer azimuth angles under different incident angles of 51° , 57° , 63° and 69° . When different measurement configurations are

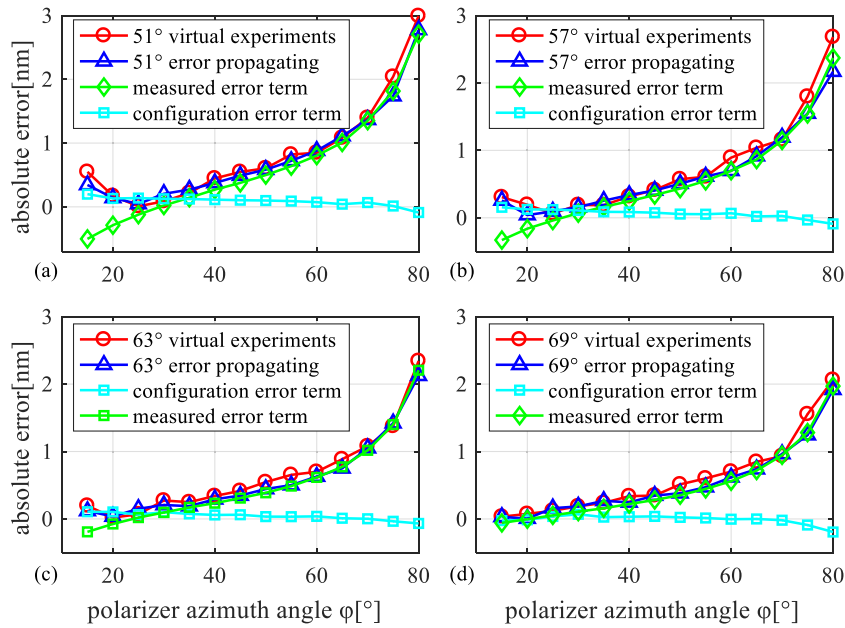


Figure 3. The comparison between the systematic errors of the thickness measurement of the SiO₂ layer exhibited in virtual experiments and those calculated by the systematic error propagating model: (a) $\theta = 51^\circ$, (b) $\theta = 57^\circ$, (c) $\theta = 63^\circ$, (d) $\theta = 69^\circ$. Red open circles: the imitated systematic error obtained from the virtual experiments. Blue upside-down triangles: the calculated systematic error obtained from the systematic error propagating formula shown as equation (17). Brilliant blue square: the calculated errors component induced by the configuration parameters errors. Green rhombus: the calculated errors component induced by the intrinsic errors of Stokes parameters.

applied, significant changes in the imitated systematic error $\langle \Delta \mathbf{x} \rangle$ can be observed. Moreover, the variations of imitated errors $\langle \Delta \mathbf{x} \rangle$ demonstrate good consistency with that of the calculated error $\mu_{\mathbf{x}}$. Such results demonstrate the validity of the systematic error propagating formula, which serves as the basis of the proposed optimization method. Furthermore, the calculated errors components induced by the configuration parameters errors and the intrinsic errors of Stokes parameters were calculated using equation (17). The corresponding results are shown in figure 3. Although the former errors component is much less than the latter in the majority of cases, the influence of the configuration parameters errors is inevitable and cannot be ignored. In the evaluation of the systematic errors propagated into the measurand, the influence of both the configuration parameters errors and the intrinsic errors of Stokes parameters should be taken into consideration. In order to check the robustness of our method, simulation experiments with large errors were also conducted. For example, the biases of systematic parameters are set as large as $\Delta \mathbf{a} = [\Delta \theta, \Delta \varphi]^T = [0.4^\circ, 0.4^\circ]^T$ and $\Delta \mathbf{b} = [0.4^\circ, 0.4^\circ, 0.4^\circ, 0.4^\circ]^T$, respectively. Although the absolute values of the errors are larger, the variations of the imitated errors $\langle \Delta \mathbf{x} \rangle$ still demonstrate good consistency with those of the calculated error $\mu_{\mathbf{x}}$.

Next, we further predict the optimal measurement configurations for the thickness measurement of a SiO₂ layer as a case study. Since the nominal thickness of the sample is 32 nm, we assume the real thickness of the sample is in the interval of [29.3, 35.1] nm. Supposing the incident angle θ varies from 45° to 72° and the azimuth angle φ of polarizer P₂ is changing from 19° to 69° with an increment of 5°, the Frobenius norm of $\left[(\mathbf{J}_x^T \mathbf{W} \mathbf{J}_x)^{-1} \mathbf{J}_x^T \mathbf{W} \mathbf{J}_a (\mathbf{J}_x^T \mathbf{W} \mathbf{J}_x)^{-1} \mathbf{J}_x^T \mathbf{W} \right]$ can

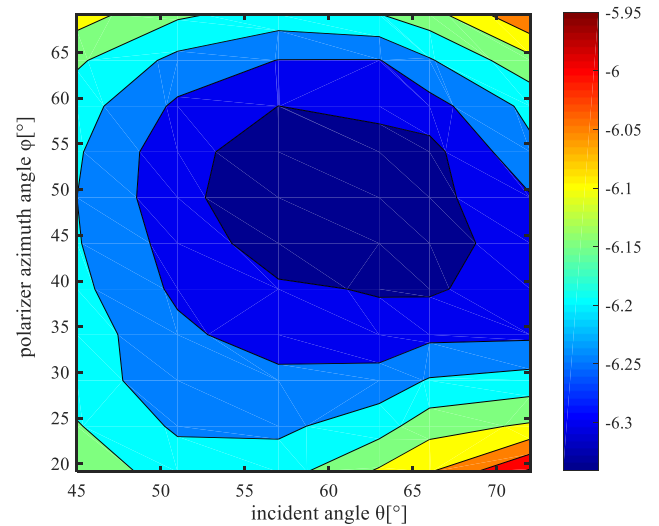


Figure 4. The natural logarithms of the objective function under different measurement configurations. The objective function is shown as equation (19).

be calculated. Figure 4 shows the calculated maximal values of $\left\| (\mathbf{J}_x^T \mathbf{W} \mathbf{J}_x)^{-1} \mathbf{J}_x^T \mathbf{W} \mathbf{J}_a (\mathbf{J}_x^T \mathbf{W} \mathbf{J}_x)^{-1} \mathbf{J}_x^T \mathbf{W} \right\|_F$ under different configurations. Based on the optimization model shown in equation (19), the objective of the optimization is to determine an appropriate combination of θ and φ which can minimize the maximal value of the systematic error. The combination of θ and φ corresponding to the minimum value of the objective function shown in figure 4 would be the optimal configuration for the test case.

In order to clearly show the changes of the objective function with respect to different configuration conditions, we

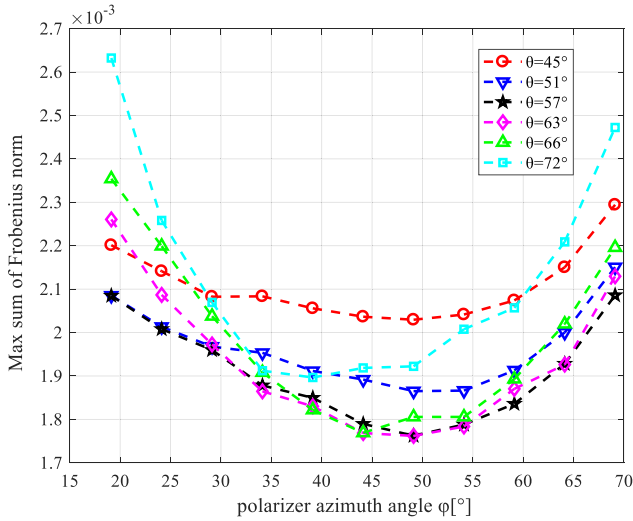


Figure 5. Maximal sum curves of the Frobenius norm of the propagation coefficient matrix of SiO₂ under the incident angle θ of 45°, 51°, 57°, 63°, 66° and 72° and the varying azimuth angle φ of polarizer P₂. The propagation coefficient matrix is shown as equations (18) and (19).

fixed the incident angle as 45°, 51°, 57°, 63°, 66° and 72° and allowed the polarizer azimuth angle to vary. Figure 5 shows the objective function changes induced by the azimuth angle variation. As shown in figure 5, the predicted optimal configuration is the combination of the incident angle of 63° and the polarizer azimuth angle of 49°. In addition, since the objective function at $\theta = 57^\circ$ and $\varphi = 49^\circ$ is approximately equal to the minimum value at $\theta = 63^\circ$ and $\varphi = 49^\circ$, the configuration of $\theta = 57^\circ$ and $\varphi = 49^\circ$ should be an alternative to the optimal configuration for this test case. In particular, if the incident angle is fixed as 45°, the corresponding optimal azimuth angle of polarizer P₂ is about 49°.

A practical reflected Stokes parameters and thickness measurement on a standard SiO₂ thin film was carried out using the polarimeter we developed for demonstration. For reference, the reflected Stokes parameters and the thickness of the SiO₂ thin film were first measured by a Mueller matrix ellipsometer (ME-L, Wuhan Eoptics Technology Co., Wuhan, China) and the thickness reported by the ellipsometer was 32.215 nm. The natural logarithms of relative errors in the reflected Stokes parameters measurement were calculated by equation (21.1) and are shown in figure 6(a),

$$\text{MSE}_{\text{Stokes}} = \ln \left(\sqrt{\frac{\sum_{i=0}^3 [S_{i,p} - S_{i,m}]^2}{3}} \right), \quad (21.1)$$

where $\text{MSE}_{\text{Stokes}}$ was the natural logarithms of the relative errors in the reflected Stokes parameters measurement, $S_{i,p}$ and $S_{i,m}$ were the reflected Stokes parameters measured by the polarimeter and the Mueller matrix ellipsometer, respectively.

The relative errors in the thickness measurement are calculated by equation (21.2) and are shown in figure 6(b)

$$R = \frac{d_p - d_m}{d_m}, \quad (21.2)$$

where d_p and d_m are the thicknesses measured by the Stokes polarimeter and the Mueller matrix ellipsometer, respectively.

Figure 6 shows the relative error changes of the measured Stokes parameters and the measured thickness with respect to configuration conditions. The trends of the curves shown in figure 6(a) demonstrated good consistency with those shown in figure 6(b). This is because the thickness of SiO₂ thin film is extracted from the measured Stokes parameters following equation (9). From the results shown in figure 6(a), we find that the magnitudes of the relative errors in the Stokes parameters measurement are nearly commensurate with those of the objective functions shown in figure 4, which indicates that equation (19) can provide an adequate estimation of the errors in the Stokes parameters. Compared to figure 5, similar trends of relative error changes with respect to configuration conditions can be observed in figures 6(a) and (b). The optimal incident angle and the polarizer azimuth angle are 63° and 49°, respectively, which is in great agreement with the predictions given in figure 5. It is worth noting that when the incident angle is 57° and the polarizer azimuth angle is 49° the configuration can be regarded as the secondary optimal setting, as reported in figure 5. In particular, when the incident angle is 45°, the measurement relative error could be reduced from 6% to less than 1% if an appropriate polarizer azimuth angle of 49° can be applied.

Finally, we carried out the second case study that is the metrology of a dynamic loading process. In this case, our polarimeter is applied to measure the dynamic optical constant changes of a nickel foil (nominal thickness of about 100 μm, covered by a LiF window) loaded by a pulse heating system [2, 15, 33, 34]. When a large electric current pulse was passing through the nickel foil, the surface temperature of the nickel foil could be rapidly raised from 300 K to 1800 K in less than 400 μs. Since the responses under high temperature (usually above 900 K) are critical for phase shift study, we simulated the process of the dynamic complex refractive index changes of the nickel foil by monitoring the temperature-dependence Stokes parameters when the temperature was varied from 1200 K to 1720 K. In the dynamic experiment, the temperature was assumed to be changed linearly to the time by the fine controlling of the pulse heating system. According to the results reported by [15], the optical constants of the nickel foil were changed linearly with respect to the temperature variations. Thus, the optical constants were also linearly time-dependent, as described in equation (22):

$$n = c_1 \cdot (t - t_0) + c_2, \quad (22.1)$$

$$k = c_3 \cdot (t - t_0) + c_4, \quad (22.2)$$

where c_1 , c_2 , c_3 , c_4 and t_0 are the coefficient factors, t is the heating time and n and k are the refractive index and the extinction coefficient, respectively. The measurands in this

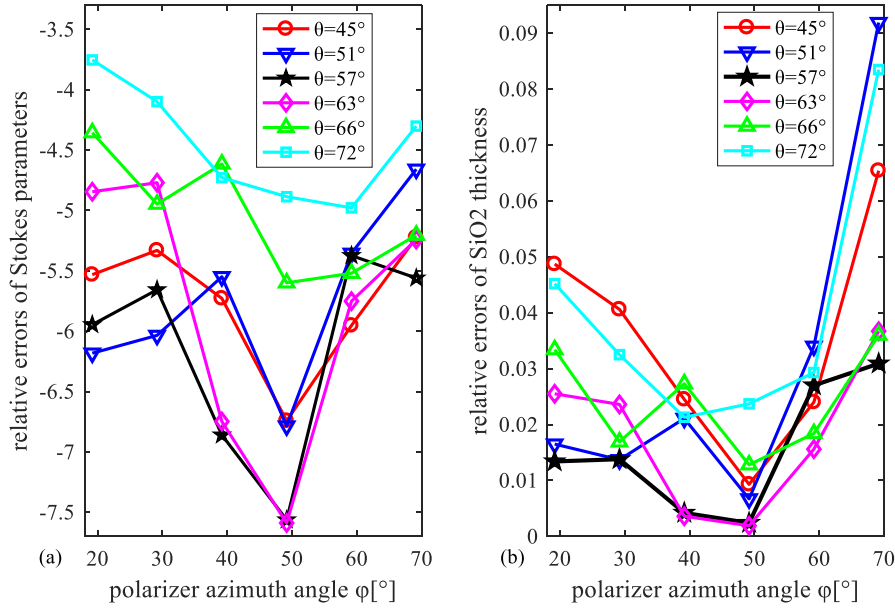


Figure 6. The relative error of the measured Stokes parameters and the measured SiO₂ thin film thickness under different configurations. (a) The natural logarithms of the relative errors of the measured Stokes parameters. (b) The relative errors of the measured SiO₂ thin film thickness.

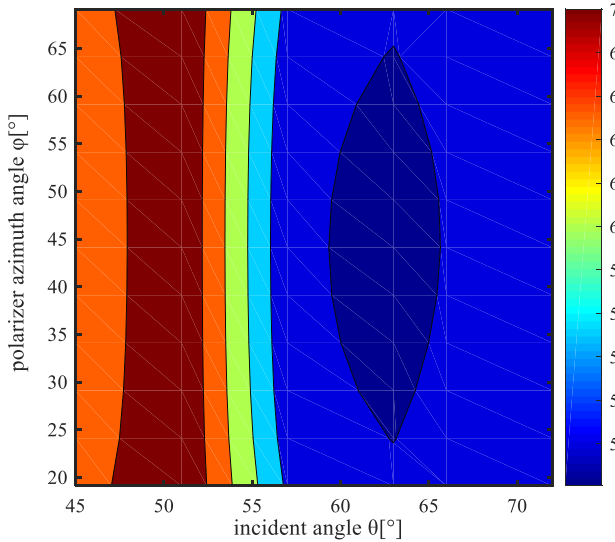


Figure 7. The natural logarithm of the calculated objective function for a dynamically loaded nickel foil under different measurement configurations. The objective function is shown as equation (19).

case have been transformed from $\mathbf{x} = [n, k]^T$ to $\mathbf{x} = [c_1, c_2, c_3, c_4, t_0]^T$ by the parameterized model. According to the results of [1200 K, 1720 K] reported in [15], the measured value of measurand \mathbf{x} is set as $[0.0013, 2.026, -0.0015, 3.435, 300]^T$.

Since c_2 and c_4 are the optical properties under normal conditions they can be regarded as constants of 2.026 and 3.435, respectively [15]. Thus, the measurands are c_1, c_3 and t_0 , i.e. $\mathbf{x} = [c_1, c_3, t_0]$ only. The reference complex refractive index of LiF is set as $N = 1.3912 - i0$ as reported in the literature [35] and assumes that the thickness of the LiF window is $2 \mu\text{m}$. The recording time varies from $300 \mu\text{s}$ to $350 \mu\text{s}$ with an increment of $0.5 \mu\text{s}$, which corresponds to the temperature range [1200 K, 1720 K]. The feasible intervals of c_1, c_3 and t_0 are defined as the

ranges of $[0.001281, 0.001320]$, $[-0.001523, -0.001478]$, and $[295.5, 304.5] \mu\text{s}$, respectively. These intervals of c_1, c_3 and t_0 represent the feasible domains of the initial values for fitting, respectively. According to the experimental results obtained between 1200 K and 1720 K reported in [15], the midpoints in the feasible intervals for c_1, c_3 and t_0 were set as 0.0013, -0.0015 and 300, respectively. The upper and lower bounds of the feasible intervals were set as 101.5% and 98.5% of the midpoints, respectively, due to the requirement for the initial values of the inverse problem. The incident angle θ varies from 45° to 72° , and the azimuth angle φ of polarizer P₂ changes from 19° to 69° , both with increments of 5° . Thus, the objective function under different configurations can be calculated and the results are shown in figure 7. The corresponding optimal measurement configuration predicted is a combination of $\theta = 63^\circ$ and $\varphi = 49.19^\circ$. It is worth noting that figure 7 exhibits not only an optimal configuration but also an optimal domain distributed in the area of $\theta = [60^\circ, 67^\circ]$ and $\varphi = [25^\circ, 65^\circ]$.

5. Conclusions

In summary, we developed a fast, low-cost and high temporal resolution Stokes polarimeter to measure the optical constants of samples under dynamic loadings. A measurement configuration optimization model has been proposed to acquire the optimal configuration based on the systematic error propagating mechanism. In order to expand the feasible domain of configuration optimization, a quarter-wave plate was inserted in front of the second polarizer to avoid the systematic error due to the extinction effect. Virtual and practical experiments for measuring the thickness of a standard SiO₂ thin film were carried out for demonstration. The optimal configuration and corresponding relative errors predicted by the optimization model are in great agreement with the results exhibited in the

practical experiments. Finally, the metrology of a nickel foil under dynamic loading was discussed and the corresponding optimal configuration with the objective of improving the measurement accuracy has been predicted. The proposed protocol herein is envisioned to pave the way for the improvement of measurement accuracy and experimental efficiency under extreme conditions, especially for those tests characterized by short duration, unrepeatability and high costs, etc.

Acknowledgments

This work was funded by the National Natural Science Foundation of China (Grant Nos. 51575214, 51525502, 51727809, 51475191 and 51775217); the National Key Research and Development Plan (Grant No. 2017YFF0204705); the China Postdoctoral Science Foundation (Grant Nos. 261M602288 and 2017T100546); and the National Science and Technology Major Project of China (Grant No. 2017ZX02101006-004).

ORCID iDs

Xiuguo Chen  <https://orcid.org/0000-0002-7067-5084>
 Hao Jiang  <https://orcid.org/0000-0003-0561-5058>
 Shiyuan Liu  <https://orcid.org/0000-0002-0756-1439>

References

- [1] Ali S J, Bolme C A, Collins G W and Jeanloz R 2015 Development of a broadband reflectivity diagnostic for laser driven shock compression experiments *Rev. Sci. Instrum.* **86** 043112
- [2] Seifert A, Sachsenhofer F and Pottlacher G 2002 A fast laser polarimeter improving a microsecond pulse heating system *Int. J. Thermophys.* **23** 1267–80
- [3] Bolme C A, McGrane S D, Moore D S, Whitley V H and Funk D J 2008 Single shot Hugoniot of cyclohexane using a spatially resolved laser driven shock wave *Appl. Phys. Lett.* **93** 191903
- [4] Hazell P J, Beveridge C, Groves K and Appleby-Thomas G 2010 The shock compression of microorganism-loaded broths and emulsions: experiments and simulations *Int. J. Impact Eng.* **37** 433–40
- [5] Rapp S, Kaiser M, Schmidt M and Huber H P 2016 Ultrafast pump-probe ellipsometry setup for the measurement of transient optical properties during laser ablation *Opt. Express* **24** 17572–92
- [6] Barker L M and Hollenbach R E 1972 Laser interferometer for measuring high velocities of any reflecting surface *J. Appl. Phys.* **43** 4669–75
- [7] Bloomquist D D and Sheffield S A 1983 Optical recording interferometer for velocity measurements with subnanosecond resolution *J. Appl. Phys.* **54** 1717–22
- [8] Strand O T, Goosman D R, Martinez C and Whitworth T L 2006 Compact system for high-speed velocimetry using heterodyne techniques *Rev. Sci. Instrum.* **77** 083108
- [9] Seagle C T and Dolan D H 2013 Note: visible reflectivity system for high-pressure studies *Rev. Sci. Instrum.* **84** 066104
- [10] Funk D J, Moore D S, Gahagan K T, Buelow S J, Reho J H, Fisher G L and Rabie R L 2001 Ultrafast measurement of the optical properties of aluminum during shock-wave breakout *Phys. Rev. B* **64** 115114
- [11] Dang N C, Bolme C A, Moore D S and McGrane S D 2011 Femtosecond stimulated Raman scattering picosecond molecular thermometry in condensed phases *Phys. Rev. Lett.* **107** 043001
- [12] Boschini F, Hedayat H, Piovera C, Dallera C, Gupta A and Carpene E 2015 A flexible experimental setup for femtosecond time-resolved broad-band ellipsometry and magneto-optics *Rev. Sci. Instrum.* **86** 013909
- [13] Rebibo S, Geindre J P, Audebert P, Grillon G and Chambaret J P 2001 Single-shot spectral interferometry of femtosecond laser-produced plasmas *Laser Part. Beams* **19** 67–73
- [14] Bolme C A and Funk D J 2008 Ultrafast dynamic ellipsometry measurements of early time laser ablation of titanium thin films *Appl. Phys. A* **92** 761–6
- [15] Bakshim L, Eliezer S, Appelbaum G, Nissim N, Perelmutter L and Mond M 2012 A full Stokes vector ellipsometry measurement system for *in situ* diagnostics in dynamic experiment *Rev. Sci. Instrum.* **83** 053904
- [16] Gross H and Rathsfield A 2008 Sensitivity analysis for indirect measurement in scatterometry and the reconstruction of periodic grating structures *Wave Random Complex* **18** 129–49
- [17] Mu T, Chen Z, Zhang C and Liang R 2016 Optimal configurations of full-Stokes polarimeter with immunity to both Poisson and Gaussian noise *J. Opt.* **18** 055702
- [18] Zallat J, Aïnouz S and Stoll M P 2006 Optimal configurations for imaging polarimeters: impact of image noise and systematic errors *J. Opt. A: Pure Appl. Opt.* **8** 807–14
- [19] Ambirajan A and Look D C 1995 Optimum angles for a polarimeter: part I *Opt. Eng.* **34** 1651–5
- [20] Sabatke D S, Descour M R, Dereniak E L, Sweatt W C, Kemme S A and Phipps G S 2000 Optimization of retardance for a complete Stokes polarimeter *Opt. Lett.* **25** 802–4
- [21] Tyo J S 2002 Design of optimal polarimeters: maximization of signal-to-noise ratio and minimization of systematic error *Appl. Opt.* **41** 619–30
- [22] Dong Z, Liu S, Chen X and Zhang C 2014 Determination of an optimal measurement configuration in optical scatterometry using global sensitivity analysis *Thin Solid Films* **562** 16–23
- [23] Logofatu P C 2002 Phase-modulation scatterometry *Appl. Opt.* **41** 7187–92
- [24] Ku Y, Wang S, Shyu D and Smith N 2006 Scatterometry-based metrology with feature region signatures matching *Opt. Express* **14** 8482–91
- [25] Germer T A, Patrick H J, Silver R M and Bunday B 2009 Developing an uncertainty analysis for optical scatterometry *Proc. SPIE* **7272** 72720T
- [26] Chen X, Liu S, Gu H and Zhang C 2014 Formulation of error propagation and estimation in grating reconstruction by a dual-rotating compensator Mueller matrix polarimeter *Thin Solid Films* **571** 653–9
- [27] Fujiwara H 2007 *Spectroscopic Ellipsometry Principles and Applications* (New York: Wiley)
- [28] Liu Y, Lo Y and Liao C 2016 Compensation of non-ideal beam splitter polarization distortion effect in Michelson interferometer *Opt. Commun.* **361** 153–61
- [29] Liu S, Chen X and Zhang C 2014 Development of a broadband Mueller matrix ellipsometer as a powerful tool for nanostructure metrology *Thin Solid Films* **584** 176–85

- [30] Chen X, Liu S, Zhang C and Jiang H 2013 Measurement configuration optimization for accurate grating reconstruction by Mueller matrix polarimetry *J. Micro/Nanolithogr. MEMS MOEMS* **12** 033013
- [31] Henn M A, Gross H, Scholze F, Wurm M, Elster C and Bar M 2012 A maximum likelihood approach to the inverse problem of scatterometry *Opt. Express* **20** 12771–86
- [32] Zhang C, Liu S, Shi T and Tang Z 2009 Improved model-based infrared reflectometry for measuring deep trench structure *J. Opt. Soc. Am. A* **26** 2327–35
- [33] Cezairliyan A 1984 A dynamic technique for measurements of thermophysical properties at high temperatures *Int. J. Thermophys.* **5** 177–92
- [34] Gallob R, Jager H and Pottlacher G 1986 A submicrosecond pulse heating system for the investigation of thermophysical properties of metals at high temperatures *Int. J. Thermophys.* **7** 139–47
- [35] Li H 1976 Refractive index of alkali halides and its wavelength and temperature derivatives *J. Phys. Chem. Ref. Data* **5** 329–528